# Characterizing the acoustic properties of the cavity cloud generated close to an air-gun array as a time-dependent effective medium

**Babak Khodabandeloo[1]** and **Martin Landrø[2]**

[1]*Department of Geoscience and Petroleum, Norwegian University of Science and Technology (NTNU), NO-7491 Trondheim, Norway, Email: babak.khodabandeloo@ntnu.no*

[2] *Department of Electronic Systems, Norwegian University of Science and Technology (NTNU), NO-7491 Trondheim, Norway, Email: martin.landro@ntnu.no*

## SUMMARY

A ghost cavity cloud consists of many small vapour cavities and appears above and around the air-guns in the source array a few milliseconds after the source is fired. Since there are dissolved gases and stable microbubbles in natural seawater, the cavities will likely contain some amount of air in addition to water vapour. The cavity cloud exists for around 10 ms depending on the size and the configuration of the array. It is well known that with increasing volume fraction of tiny bubbles within the liquid, the sound velocity of the mixture at frequencies below the resonance frequencies of the bubbles gradually drops. Depending on the volume fraction of tiny bubbles, the sound velocity in the mixture can even drop below the sound velocity of the individual constituents. Vapour content within the bubbles – or cavities – further reduces the sound velocity. We do not know whether the volume fraction of the cavity cloud is high enough to significantly drop the sound velocity, nor do we know whether the far-field acoustic recording is affected even if the sound velocity within the cavity cloud drops substantially. To answer these questions, a modified k-wave − a k-space pseudo-spectral numerical method − is used. Subsequently, the simulation results are compared to recorded field data in order to estimate a potential sound velocity drop within the ghost cavity cloud. According to this comparison, we find that the reduction in sound velocity is probably less than 10 %.

## 1. INTRODUCTION

Cavities can be formed underwater when the pressure drops below the vapour pressure or partial pressure of the dissolved gases (Mellen, 1954; Plesset, 1970). Acoustic waves emitted from air-

guns in a seismic air-gun array are reflected from the sea surface with opposite polarity. Hence the addition of reflected pressure waves can drop the hydrostatic pressure of water at some locations temporarily, which is sufficient for cavity growth and subsequent collapse. This phenomenon was first hypothesized by recording high frequency (> 10 kHz) signals in a seismic air-gun array field measurement (Landrø et al., 2011). It was further analysed (Landrø et al., 2013) and investigated based on a dedicated field experiment (Landrø et al., 2016). The ghost cavitation phenomenon in an air-gun array was numerically modelled and could successfully predict the recorded high-frequency ghost cavitation signals (Khodabandeloo et al., 2017) and the associated low-frequency component (Khodabandeloo and Landrø, 2017a). Unless the water is fully degassed, the cavities contain some amount of air in addition to the vapour phase (Neppiras, 1984; Prosperetti, 2017). It is well known that even small volume fractions of bubbles in a liquid affect sound speed and attenuation of acoustic wave propagation significantly (Commander and Prosperetti, 1989). For example, adding tiny bubbles with the fraction volume of 0.1% reduces the sound velocity of the mixture with 80%. The primary cause for this effect is that the presence of air greatly decreases the compressibility of the bubbly medium while its density is almost unaltered (Kieffer, 1977). Other than the volume fraction of the gas, bubble size distribution and the frequency of the acoustic wave also affects the sound speed in the bubbly liquid. At low frequencies (compared to the resonances of bubbles) the sound velocity is mainly a function of the volume fraction of gas (Wilson and Roy, 2008). Sound velocity in a water-vapour mixture is even smaller than a water-air mixture for the same volume fraction of vapour and air (Barclay et al., 1969; Fuster and Montel, 2015; Prosperetti, 2015, 2017). Vapour bubbles are much more labile objects compared to gas bubbles since the thermal diffusivity is much larger than mass diffusivity in most liquids including water. Hence, there are fewer and less conclusive experiments on vapour bubbles compared to gas bubbles (Prosperetti, 2017). Propagation of acoustic waves through a bubbly liquid has been studied by several researchers in the last centennial and especially during World War II to utilize underwater acoustics in submarine warfare (Domenico, 1982). The acoustic impedance mismatch between the layer of bubbly water and bubble-free water is exploited in several practical applications. Bubble curtains were deployed to prevent damage to the submerged infrastructures from shock waves due to underwater blasting or explosion (La Prairie, 1955). To mitigate the noise from pile driving activity, a bubble curtain from free rising bubbles was devised to surround the source (Würsig et al., 2000) and to shield a porpoise pool (Lucke et al., 2011). Bubble curtains

with irregular shapes were placed at the bounce point of acoustic waves from sea-surface to suppress the multiples (Ross et al., 2005).

The ghost cavity cloud has the potential to locally and temporarily change the medium properties in terms of sound velocity and attenuation. There are two questions in this regard:

1. Whether the cavity cloud changes the sound velocity of water and by how much it does.
2. If the cavity cloud changes the sound velocity of water, is the far-field acoustic recording affected by such a short duration and local change in the sound velocity?

An affirmative answer to the second question opens the path to answer the first question by comparing the modelled and recorded far-field signatures. Subsequently, it might be possible to further characterize the ghost cavity cloud with regard to the sound velocity variations, average size and number of cavities.

If the resonances of bubbles within the cloud are much higher than the frequency of the propagating acoustic wave, the cloud can be considered as a uniform medium with effective acoustic properties such as sound speed and attenuation (Leighton, 1994, pp 258-278). The macroscopic properties of an effective medium are linked to the characteristics and relative fractions of its constituent components (Lee et al., 2011). To investigate the acoustic properties of the ghost cavity cloud, we use numerical methods. It is possible to discretize either the second-order acoustic wave equation or a set of coupled equations based on conservation of mass, momentum, and equation of state (Liu, 1998). Discretizing and solving a set of coupled first order equations makes it easier to include mass and force sources and to include a perfectly matched layer (PML) around the computational domain. PML absorbs the acoustic waves that reach the boundaries of the computational domain and avoids that waves are reflected back. k-wave is an efficient MATLAB toolbox which solves three coupled first-order partial differential equations for acoustic wave propagation (Treeby and Cox, 2010; Treeby et al., 2012). It uses k-space and pseudo-spectral method for temporal and spatial discretization, respectively. k-space pseudo-spectral algorithm is more efficient than many of finite difference and finite element methods because it provides the same degree of accuracy with much coarser grid spacings and larger time steps (Tabei et al., 2002; Cox et al., 2007).

In this paper, we numerically study the effects of sound velocity reduction within the ghost cavity cloud on the far-field acoustic measurements using the k-wave MATLAB toolbox. Since the ghost cavity cloud appears for only a few milliseconds, it requires a simulation of the acoustic wave propagation within a non-stationary (time-dependent) medium. The ghost cavity cloud is introduced into the numerical model to change locally and temporarily the acoustic sound speed of the medium (water). It is assumed that the resonance frequencies of the gas/vapour cavities within the cloud are higher than the propagating acoustic waves and that the acoustic attenuation of the cloud can be neglected. The simulation results are compared to recorded far-field data and the sound velocity within the ghost cavity cloud is estimated.

## 2. VISUALIZING GHOST CAVITY CLOUD

A dedicated field experiment was conducted in 2011 offshore Congo to video-record the ghost cavity cloud. The source array used in the field test was towed at 9m depth and consists of two sub-arrays with 8m horizontal separation. More details are given by Landrø et al. (2016). Part of one of the sub-arrays is video-recorded by a high-speed camera mounted on the other sub-arrays. The recording speed was 120 fps and four successive frames from one source firing are shown in Figure 1.
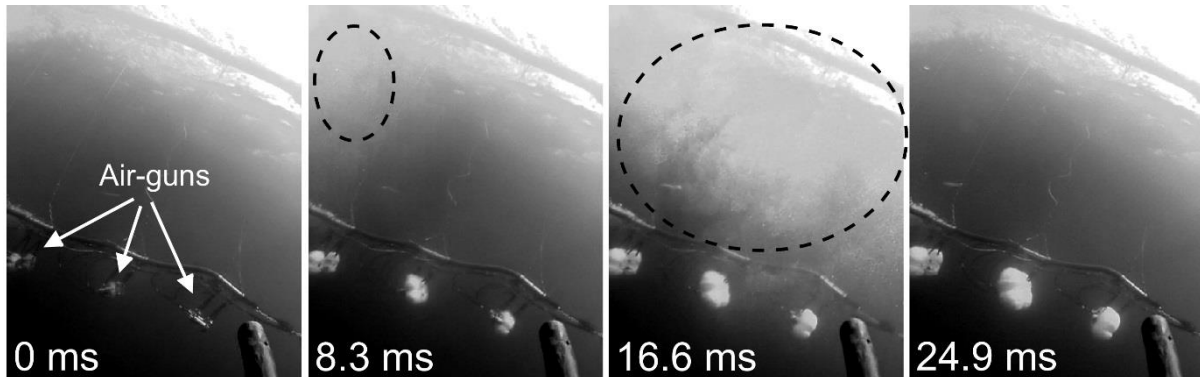


Figure 1 – Four successive frames from video recordings of one the sub-arrays with recording speed of 120 fps. The first image (0 ms) is the first frame when the air is observed escaping air-guns. Cavity clouds are indicated by dashed ellipse. The distance between two adjacent air-guns is around 2.7 m.

The cavity cloud appears partly in the second and mainly in the third frame after the guns were fired as shown in Figure 1. A hydrophone was mounted 17 m beneath the array to record the acoustic signals. However, since the recorded acoustic signals in this experiment were saturated in some parts, they are not appropriate to be compared with the modelled signals. Details of the

photographed cavity cloud and the recorded acoustic signal is given in (Khodabandeloo and Landrø, 2018).

## 3. THEORY: SPEED OF SOUND IN GAS/VAPOUR MIXTURE:

The sound speed in a fluid medium, $c$, is defined as $c = \sqrt{K/\rho}$ , where $K$ is the bulk modulus (or incompressibility) and $\rho$ is the density. Wood (1946) derived these quantities to determine the acoustic propagation sound velocity in two-fluid media such as water containing tiny air bubbles. He assumed that the mixture medium was a homogenous medium with a mean density and a mean elasticity and expressed the Wood's equation to estimate the sound velocity of the mixture as (Wood, 1946. Page 360-363):

$$c_m = \sqrt{\frac{K_m}{\rho_m}} = \sqrt{\frac{K_l K_g}{(\beta K_l + (1-\beta)K_g)(\beta \rho_g + (1-\beta)\rho_l)}}, \tag{1}$$

The volume fraction of the gas phase (or void fraction) is given by $\beta = V_g/(V_l + V_g)$, where $V_g$ and $V_l$ represent the gas and liquid volumes in the mixture, respectively. The above equation is valid for a mixture of any two fluids which do not react chemically. Furthermore, the air-bubbles should be non-resonant. In other words, it is valid for frequencies well below the resonance frequency of the air-bubbles (Silberman, 1957).

Wave propagation through a bubbly medium was considered as a problem of multiple scattering of waves by randomly distributed scatterers (Foldy, 1945). Effective medium is used instead of the complex system of a host medium containing scatterers. Including bubble dynamics and effects of bubble oscillations in the wave propagation through a bubbly medium, the following dispersion relation is derived for the averaged complex wave number of propagating wave in the mixture (Van Wijngaarden, 1972; Commander and Prosperetti 1989):

$$\frac{k_m^2}{\omega^2} = \frac{1}{c_l^2} + 4\pi \int_0^\infty \frac{R_0 f(R_0) dR_0}{\omega_N^2 - \omega^2 + i2\omega\delta}. \tag{2}$$

In the above equation, $k_m$ is the effective wave number in the mixture, $c_l$ is the sound velocity in the liquid without scatterers, $\omega_N$ is the natural frequency of the bubbles, $\omega$ is the angular frequency of the propagating wave, $\delta$ is the bubble dynamic damping constant, and $R_0$ is the equilibrium

bubble radius. The probabilistic function for the size distribution at bubble equilibrium is given by $f(R_0)$, and $f(R_0)dR_0$ gives the number of bubbles per unit volume with the equilibrium radius between $R_0$ and $R_0 + dR_0$. In deriving the above equation it is assumed that the gas volume fraction (or void fraction) is small ($\beta \ll 1$). The void fraction can be estimated as (Commander and Prosperetti, 1989):

$$\beta = \frac{4}{3}\pi \int_0^\infty R_0^3 f(R_0) dR_0 \tag{3}$$

The wavenumber in equation (2) is complex valued and the phase speed of the mixture is obtained as $c_m = \omega/Re(k_m)$.

If the frequency of the pressure perturbation is below the resonance frequency of the bubbles, equation (2) can be simplified to (Prosperreti, 2015, Equation (4.10)):

$$\frac{1}{c_m^2} = \frac{1}{c_l^2} + \frac{\beta \rho_l}{p_{g0}} \frac{1}{1 - 2\sigma/(3R_0 p_{g0})}, \tag{4}$$

where $p_{g0}$ is the equilibrium pressure inside the bubble and $\sigma$ is water surface tension. In many situations, bubbles in the liquid contain a mixture of gas and vapour. The formed cavities in a gas-free liquid should be vaporous (Neppiras, 1984). However, liquids in most practical situations contain some dissolved gas such as air. The dissolved gas in the liquid diffuses into the vapour cavity (or bubble) as it grows (Plesset, 1970; Prosperetti, 2017). Hence, usually there are some amounts of gas such as air inside the cavities. Furthermore, in many practical situations, microbubbles distributed in the liquid act as cavitation nuclei sites. In the sea water of depth up to 36 m, there are uniformly distributed microbubbles with the size between 18 μm to 350 μm when the wind speed is around 6 knots (Medwin, 1977). Vapour content changes the resonance frequency of bubbles and also reduces the speed of wave propagation in the frequency range below the resonance frequency of the bubbles (Fuster and Montel, 2015; Prosperetti, 2015, 2017; Zhang et al., 2017). When the bubbles contain vapour, at the low frequency limits the sound speed in the bubbly liquid is estimated (Fuster and Montel, 2015, Eq. (6.10)) to be:

$$c_m^2 = \frac{c_l^2}{1 + \dfrac{c_l^2 \beta \rho_l}{(1 - Y_0)p_{g0}}}$$

(5)

In equation (5), $Y_0$ is the vapour fraction inside the bubbles with gas/vapour mixture contents. Based on the above formulas the speed of sound at low frequencies in a bubbly liquid with gas/vapour mixture as a function of void fraction is shown in Figure 2.
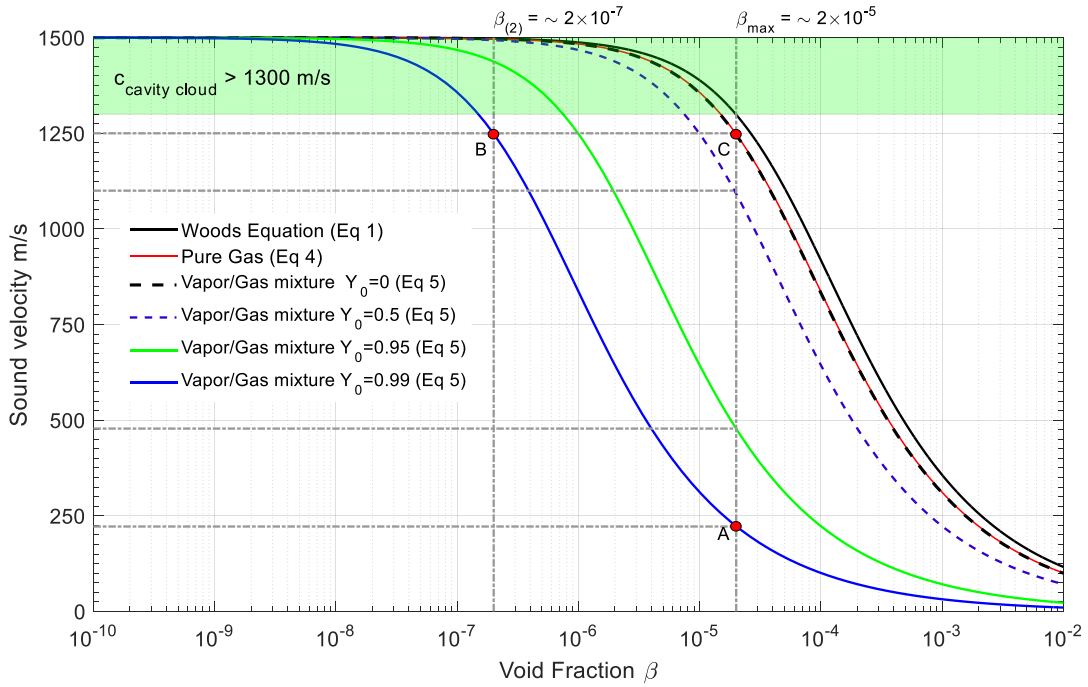


Figure 2 – Sound velocity of water with gas and gas-vapour bubbles (or cavities) for the frequency range below the resonance frequency of bubbles. Wood's equation and equation (4) for gas bubbles have a good agreement. Furthermore equation (5) with zero vapour fraction coincides to the curve for water with pure gas bubbles. The green rectangle, the vertical and horizontal dotted-dashed lines, red dots (A,B, and C), $\beta_{max}$ and $\beta_{(2)}$ are discussed in the discussion section.

The above estimations are valid for wave propagation within a bubbly medium provided that resonance effects are negligible. That is the propagation frequency should be below all resonance frequencies for uniform bubble size distribution or below the resonance frequency of bubbles with predominant size distribution (Commander and Prosperetti, 1989).

## 4. FIELD EXPERIMENT

The field experiment was performed in December 2008 in the Black Sea offshore Turkey in an area with a water depth of around 60 m. The signals were recorded using a stationary hydrophone located at the seabed. The source vessel towed the air-gun array at 5 m depth and sailed along a straight line with approximately 39 m crossline offset with respect to the recording hydrophone. The shot interval was 25 m. The side and front view of this field measurement are schematically shown in Figure 3 (left). The sea state was calm during the experiment (Landrø et al. 2013). The air-gun array configuration used for the recorded data that we refer to as field data in this paper is shown in Figure 3 (right). Operating pressure of all the guns was 2000 psi (137 bar) and they were fired simultaneously, according to the plan.
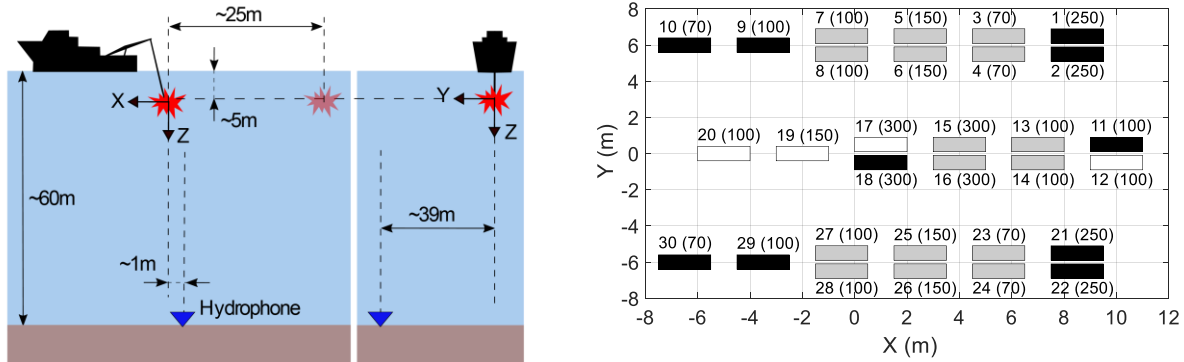


Figure 3 – (Left): Schematic side (xz) and front (yz) view of the field measurement; (Right): Air-gun array configuration used in the field experiment. Each air-gun air chamber volume (in$^3$) is given in the parentheses next to the air-gun number. The single guns are shown by white rectangle. The gray and black rectangles show cluster and inactive air-guns, respectively. In each array, the x-offset between air-guns is 3 m and the y-offset between two guns in a cluster is 1 m. The x-offset (horizontal distance) between the air-gun 1 and 11 is 1.5 m.

Aligning x-axis of the Cartesian coordinate system along the sailing line, for the closest distance between shot and the hydrophone, is an x-offset estimated to be around 1 m.

# 5. NUMERICAL IMPLEMENTATION OF WAVE PROPAGATION IN TIME-DEPENDENT MEDIUM – K-WAVE SIMULATIONS

## 5.1. Governing equations and K-wave implementation

The simulations are performed using a 3-D computational domain k-wave Toolbox (Treeby and Cox, 2010; Treeby et al., 2012) which is an open source code based on k-space pseudo-spectral

method. Instead of solving a single second-order partial differential wave equation, the simulation functions in k-wave solve the three coupled first-order partial differential equations based on conservation of mass, momentum, and equation of state relating acoustic pressure to density fluctuations. For the linear and lossless wave propagation the equations are:

Conservation of mass:

$$\frac{\partial \rho'}{\partial t} + \nabla \cdot (\rho_0 \mathbf{v}) = S_M. \tag{6}$$

Density fluctuations are denoted by $\rho'$, the particle velocity vector by $\mathbf{v}$, the ambient (or equilibrium) density by $\rho_0$ and the mass source term by $S_M$, which represents the time rate of input mass per unit volume (kg/m$^3$s). Conservation of momentum (Euler equation) yields:

$$\frac{\partial \mathbf{v}}{\partial t} + \frac{1}{\rho_0} \nabla p' = S_F. \tag{7}$$

In the above equation $S_F$ is the force source term with units of N/kg or m/s$^2$ and represents the body forces per unit mass. The equation of state is given as

$$p' = c^2 \rho'. \tag{8}$$

Equation (8) is valid for time-independent sound velocity $c$. The ghost cavity cloud (see Landrø et al., 2016 and Khodabandeloo et al. 2017) is formed by several cavities that grow and collapse for a short period of time in the vicinity of the seismic air-gun array where the pressure drop is sufficiently large to trigger vapour cavity generation. The acoustic properties of regions where vapour cavities appear might change and therefore the governing wave equations should accommodate a *time dependent medium*. This means that the equation of state (equation (8)) should be replaced by an appropriate equation to include a time varying sound speed. For isentropic flow (Ds/Dt = 0) the equation of state is (Pierce, 1981, chapter 1; Rienstra and Hirschberg, 2015, pp. 15–19, 68–70):

$$p = p(\rho, s) \Rightarrow \frac{Dp}{Dt} = \left(\frac{\partial p}{\partial \rho}\right)_s \frac{D\rho}{Dt}. \tag{9}$$

Where $s$ represents entropy. The above equation can be rewritten as:

9

$$\frac{\partial(p' + p_0)}{\partial t} + v'.\nabla(p' + p_0) = c^2\left(\frac{\partial(\rho' + \rho_0)}{\partial t} + v'.\nabla(\rho' + \rho_0)\right) \qquad (10)$$

Ignoring the second order term and taking into account that the presence of cavities might change the sound speed while the change in the ambient density is negligible, equation (10) is simplified to the following equation:

$$\frac{\partial p'}{\partial t} = c^2\frac{\partial \rho'}{\partial t}. \qquad (11)$$

The air-gun array (Figure 3) used for the field experiment is almost symmetric around the y=0 plane. It is possible to exploit this symmetry to reduce the size of the computational domain by introducing a slight position change for guns 12 and 17. Figure 4 shows the source used in the reduced computational domain with y=0 plane as a sound hard boundary condition (shown by dashed blue). For practical implementations, guns 12, 17, 19, and 20 are placed on the node in y-direction adjacent to the sound hard boundary plane, not on it. Since the sound hard boundary condition acts as a mirror, the strengths of these air-guns are scaled by 0.5 as indicated in Figure 4.
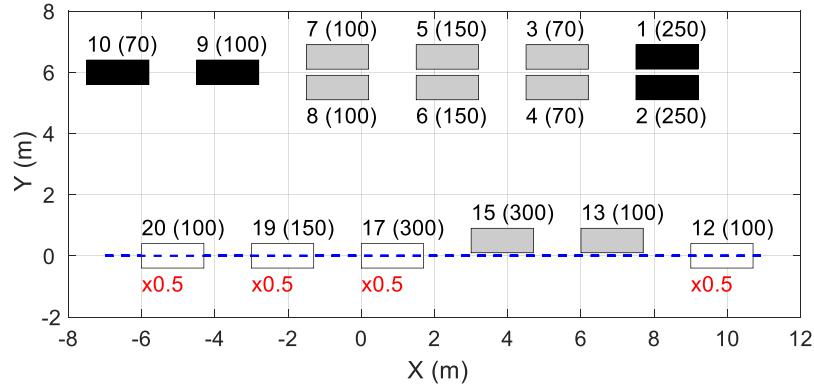


Figure 4 – The source array configuration used in numerical modelling with half space computational domain exploiting the symmetry of the source array used in the field experiment. The symmetry plane is shown by the dashed blue line. Since the symmetry plane is modelled as a sound hard boundary condition, the strength of the single air-guns located on this plane are scaled by 0.5 (See also Figure 3 (Right)). In practice the sources are not placed exactly on the sound hard plane; they are placed on the next node in the y-direction.  Air-guns 12 and 17 are shifted slightly in the y-direction. The distances between air-guns are given in the caption of Figure 3.

The 3D computational domain is shown in Figure 5 with grid numbers Nx=192, Ny=256, and Nz=384 in x, y, and z directions, respectively. The grid-point spacing ($\Delta x = \Delta y = \Delta z$) in all dimensions is 0.2 m. Since each air-gun is placed on a grid-point, considering the configuration of the air-gun array given in Figure 3 (right), some of the air-guns are shifted $\pm 0.1$ m to accommodate the grid resolution in Figure 4. To observe how the modelled far-field acoustic pressures are influenced by such shifts in the air-gun positions, the simulated far-field acoustic pressure from the source shown in Figure 4 using k-wave and the one from full air-gun array (shown in Figure 3 (Right)) modelled by NUCLEUS[TM] are plotted in Figure 6 (a), i.e. line (i) and (iv), respectively. In both models, there is no sea-floor below the hydrophone. It is observed that the slight shifts in the air-gun positions have a negligible effect on the far-field signature. Sound velocity of water is selected as 1500 m/s and the density is 1000 kg/m$^3$.
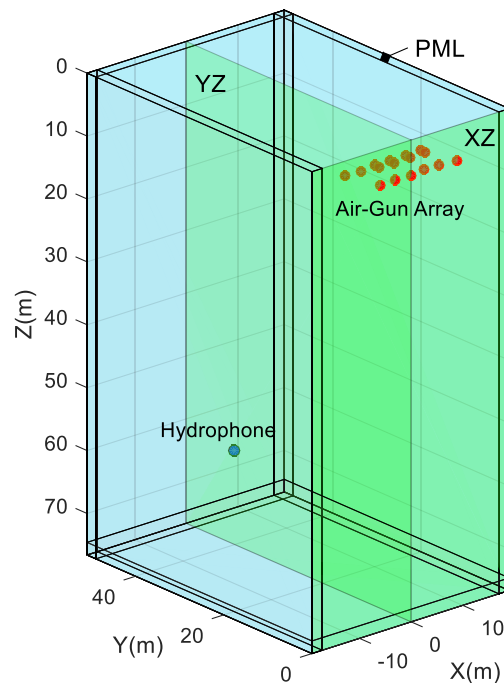


Figure 5 – The computational domain for k-wave method. The source array and receiver (hydrophone) are shown. The (Y=0) plane is the pressure sound hard boundary condition and plane (Z=0) is the pressure release boundary condition. The boundaries are surrounded by a perfectly matched layer (PMLs)

The time step for iteratively solving the equations (2), (6), and (11) based on k-space pseudo-spectral method is obtained using Courant–Friedrichs–Lewy (CFL) number equal to 0.3, where $\Delta t = CFL.\Delta x/c_{max}$ (Treeby et al., 2012). $c_{max}$ is the maximum value of the sound speed in the medium. Based on the selected parameters the time step is 40 μs and the maximum supported frequency is 3.75 kHz. The acoustic pressure emitted from each air gun in the array is modelled by the NUCLEUS$^{TM}$ source modelling package from Petroleum Geo-Services (PGS) and the output from this modelling is used as the mass source term in (6). The finest time resolution of the modelled source signatures by NUCLEUS$^{TM}$ is 0.5 ms. Therefore, the source signatures were interpolated using a piecewise cubic Hermite interpolating polynomial MATLAB function to obtain a time intervals of 40μs, which is required by k-wave algorithm. To prevent the reflections from the edge of the simulation region, the computational domain is surrounded by a Perfectly Matched Layer (PML) with 10 grid points thickness at each side as shown in Figure 5. Using first order coupled equations is convenient for PML implementation (Treeby and Cox, 2010). The Z=0 plane is the pressure release boundary condition simulating the sea-surface. To exploit the symmetry of the problem and solve it in the reduced computational domain, the Y=0 plane is the pressure sound hard boundary condition.

## 5.2. Effects of layered sea-floor on the recorded pressure

In Figure 6 (a), line (i) shows the simulated acoustic pressure at the hydrophone location using k-wave for the case when there is no sea-floor (i.e. in Figure 6(b), $\rho_1 = \rho_2 = \rho_3 = 1000\ kg/m^3$ and $c_1 = c_2 = c_3 = 1500\ m/s$). It is seen that the amplitude of simulated acoustic pressure is smaller than the amplitude of field recorded pressure while their shape has a reasonable agreement. In Figure 6 (a), line (ii) shows the simulated far-field acoustic pressure for the case when a one-layer sea-floor is included beneath the hydrophone. It seems reasonable to select the density and sound velocity of the sea-floor sediments as 1600 kg/m$^3$ and 1600 m/s, respectively (Hamilton, 1978; Nobes et al., 1986). Therefore, in this case $\rho_1 = 1000\ kg/m^3, \rho_2 = \rho_3 = 1600\ kg/m^3$ and $c_1 = 1500\ m/s,\ c_2 = c_3 = 1600\ m/s$. Compared to the previous case, the amplitude of the simulated signal is increased and the match between the simulated and field recorded far-field pressure signatures is improved. Even though adding a one-layer sea-floor beneath the hydrophone increases the amplitude of the simulated acoustic pressure at the hydrophone location, its shape is unaffected compared to the no sea-floor case as seen by plotting the normalized pressure signatures

of these two cases in Figure 6 (c). However, the influence of the sea-floor should appear 80 ms after the main peak. This 80 ms (=2×60/1500 s) is the required time for the reflected pressure from sea-floor to reach the sea-surface and be reflected back to the hydrophone. To see the effects of layered sea-floor on the recorded signal by the hydrophone on the sea-floor, it is assumed that 8 m below the sea-floor there is a change in acoustic properties of the medium. The density of the layer 8 m below the sea-floor is assumed to be 1700 kg/m$^3$ and its sound velocity is 1700 m/s. That is, for the two-layer sea-floor: $\rho_1 = 1000\ kg/m^3, \rho_2 = 1600\ kg/m^3$, $\rho_3 = 1700\ kg/m^3$ and $c_1 = 1500\ m/s,\ c_2 = 1600\ m/s,\ c_3 = 1700\ m/s$.
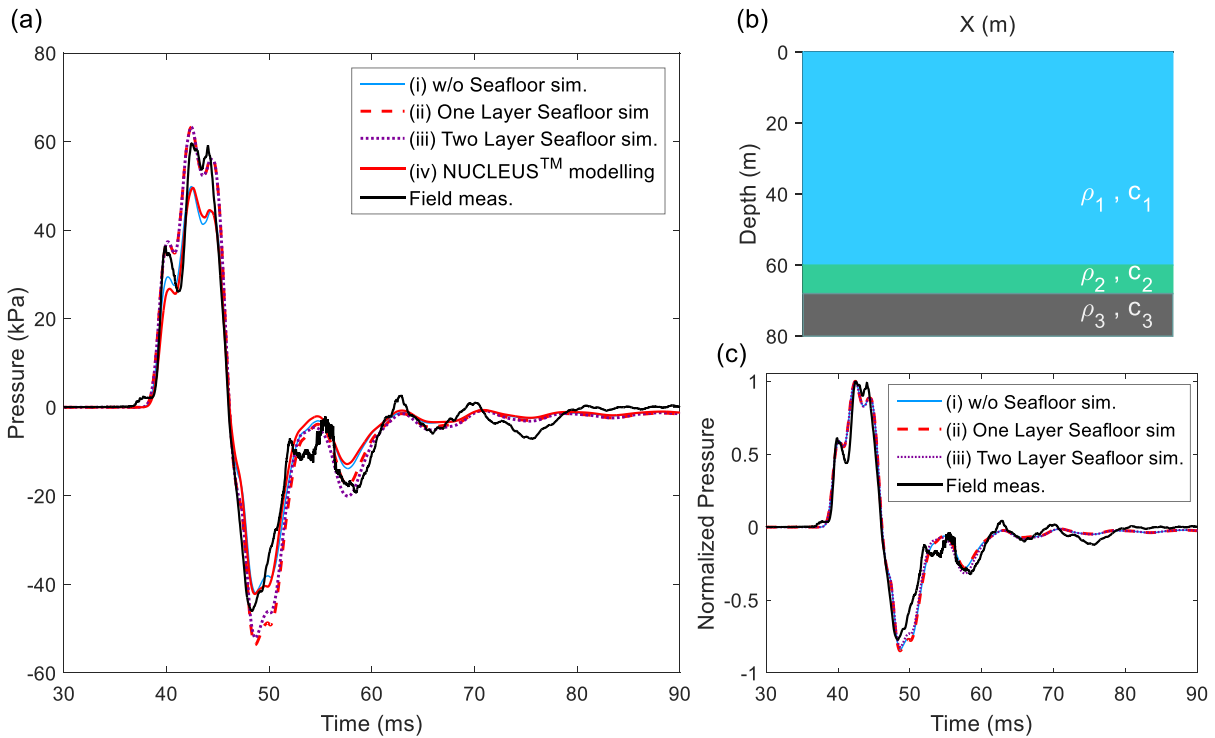


Figure 6 – (a): Field recorded acoustic pressure signature is plotted together with the simulated far-field for different simulation scenarios (i) without sea-floor, (ii) one-layer sea-floor, and (iii) two-layer sea-floor. The scenarios depend on the selected values for density and sound velocities of layers shown in (b). i) no sea-floor: $\rho_1 = \rho_2 = \rho_3 = 1000\ kg/m^3$ and $c_1 = c_2 = c_3 = 1500\ m/s$, ii) one-layer sea-floor: $\rho_1 = 1000\ kg/m^3, \rho_2 = \rho_3 = 1600\ kg/m^3$ and $c_1 = 1500\ m/s,\ c_2 = c_3 = 1600\ m/s$ , iii) two-layers sea-floor: $\rho_1 = 1000\ kg/m^3, \rho_2 = 1600\ kg/m^3$, $\rho_3 = 1700\ kg/m^3$ and $c_1 = 1500\ m/s$, $c_2 = 1600\ m/s, c_3 = 1700\ m/s$. Pressure signature simulated by NUCLEUS$^{TM}$ for the full air-gun array when there is no sea-floor is plotted (line (iv)). The normalized simulated far-field pressure

signatures for different scenarios are plotted together with the normalized field recorded pressure signature in the Sub-figure (c). There is no reflection from the bottom of the third layer.

For the given two-layer sea-floor, the simulated acoustic pressure is plotted by line (iii) in Figure 6 (a) and its normalized version is plotted in Figure 6 (c). It is seen that the two-layer sea-floor has a small effect on the simulated signal. By selecting appropriate values for the density and sound velocity of sea-floor, it is possible to have the same amplitude of the simulated pressure signature as the field recorded one. Therefore, we have scaled the signals to have the same amplitude as field recorded pressure signature for the nearest hydrophone and plotted in Figure 7 (left) for the cases without sea-floor and with two-layer sea-floor. Using the same scaling for the model, the simulated pressure signatures of these two cases are plotted for the next two shots in Figure 7 middle and right.
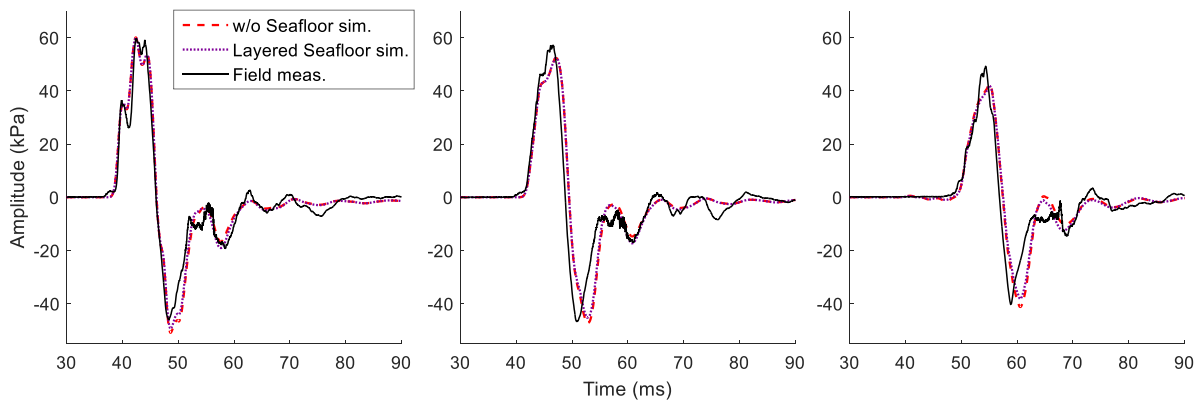


Figure 7 – Comparison of simulation results without sea-floor, with a two-layer sea-floor and the field measurements for three shot-receivers: (Left) closest shot receiver when the air-gun array has passed (x=1.2 m); (Middle) next shot after closest shot-receiver. The air-gun array is 26.2 m after the hydrophone (x=26.2 m); (Right) air-gun array is 51.2 after the hydrophone (x=51.2 m).

The simulation results indicate that including a layered sea-floor with selected acoustic properties has an insignificant effect on the recorded pressure by the hydrophone located at the sea-floor. The selected acoustic properties seem to be realistic since the simulation in the paper refers to areas with the presence of typical seafloor sediments.

## 5.3. Effects of local time-dependent medium around the source array

We assume a ghost-induced cavity cloud being represented by an ellipsoid with dimensions (Rx=6 m, Ry=5 m, Rz=3.5 m) centred one meter above the centre of an air-gun array. The array depth is

5 m and with a configuration as shown in the right side of Figure 3. In this section, we want to numerically study the effects of a temporarily sound velocity drop within the ellipsoid on the received acoustic pressure at a receiver array beneath the source. In this example, we assume that the sound velocity within the ellipsoid drops to 500 m/s 11 ms after the air-gun array is fired and raises back to 1500 m/s 8 ms later. The array consists of 18 receivers and are arranged along a line 30 m below the source array in the x-direction with 5 m spacing between two successive receivers. This means that the x-offset between array centre and the first receiver is zero and it is 85 m for the eighteenth receiver. The received acoustic signals at 18 receivers in a stationary medium (i.e. no change in the medium properties) and in a time-dependent medium are modelled and plotted after normalization by solid blue and red dashed lines, respectively, in Figure 8 (left). The difference between these two simulated signals for each receiver is shown in Figure 8 (right) without normalization. This figure shows the net effect of the sound velocity drop within the ellipsoid on the acoustic pressure recorded by the receiver array. For the given source array, the assumed ellipsoid dimension, and the assumed sound velocity drop within the cloud for the given time duration, the amplitude of pressure fluctuations is between 16-25% of the array signature peak amplitude at different receiver locations.
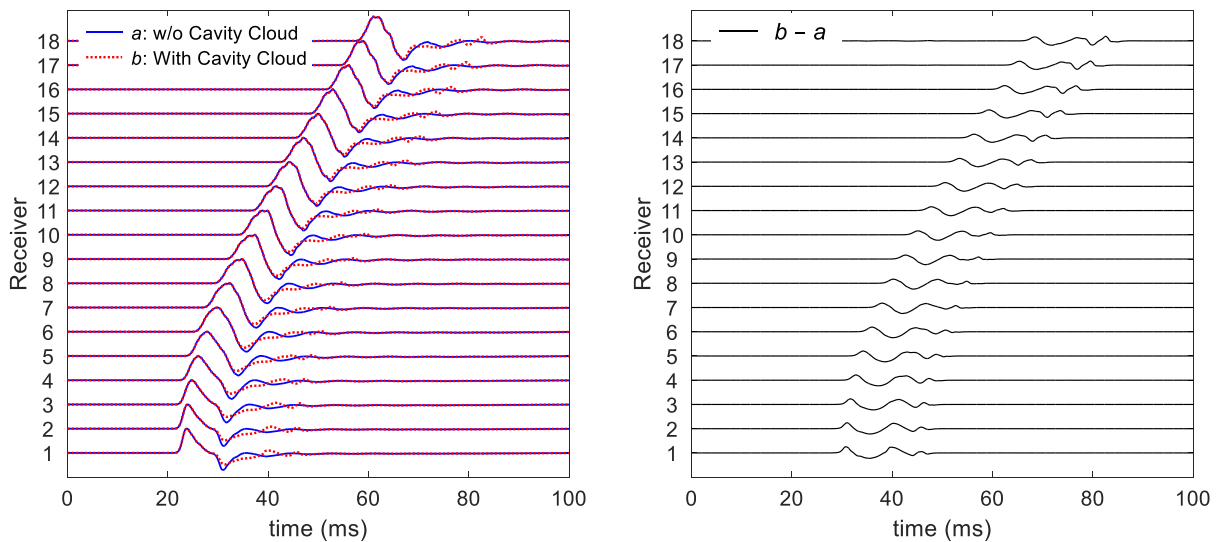


Figure 8 – (Left) Modelled acoustic pressure received by an array at different receivers without (solid blue) and with (dashed red) temporary sound velocity drop within an ellipsoid around the source array. The ellipsoid dimensions are (Rx=6 m, Ry=5 m, Rz=3.5 m) and is centred at (Cx=0, Cy=0, Cz=4 m).

All curves are normalized to one. (Right) Difference between the blue and red curves shown in the left. These are the effects of temporarily sound velocity drop within the ellipsoid.

It is observed that in both figures the arrival time of acoustic waves has the expected hyperbola shape.

## 6. RESULTS

Two different methodologies are used to include the effects of vapour cavities in the numerical simulation of recorded pressure from a seismic air-gun array. (1) Vapour cavities temporarily drop the sound velocity within a fixed ellipsoid, and (2) the pressure field around the air-gun array is modelled based on air-gun array modelling and sound velocity drops at those regions where pressure drop fulfills the requirements for cavity generations. The obtained results based on these two methodologies are presented in the following sections.

### 6.1. Cavity cloud as a fixed ellipsoid

An ellipsoid with dimensions (Rx=6 m, Ry=5 m, Rz=3.5 m) centred at (Cx=0, Cy=0, Cz=4 m) fixed in the space is shown in Figure 9 (left) representing the collection of cavities as an effective medium. For the given array configuration (Figure 3), the cavity cloud appears ~10 ms after the air-guns are fired (Figure 4 in Khodabandeloo et. al., 2017) and considering 4-5 ms average cavity lifetime, it lasts for around ~8 ms. Since the air-gun signatures modelled by NUCLEUS$^{TM}$ are zero for around ~1-2 ms before they are fired, the sound velocity of the ellipsoid drops between 12 to 20 ms to have the correct cavity cloud timings relative to the air-gun firing. Using a step function to change the sound velocity causes numerical instabilities. Therefore, the sound velocity drop and subsequent rise occur within a short time with a sigmoidal shape function. Such a sound velocity drop for four different values is shown in Figure 9 (right). As seen for one of the cases shown by the dashed blue line the sound velocity within the cloud does not change and remains at 1500 m/s in the simulation.
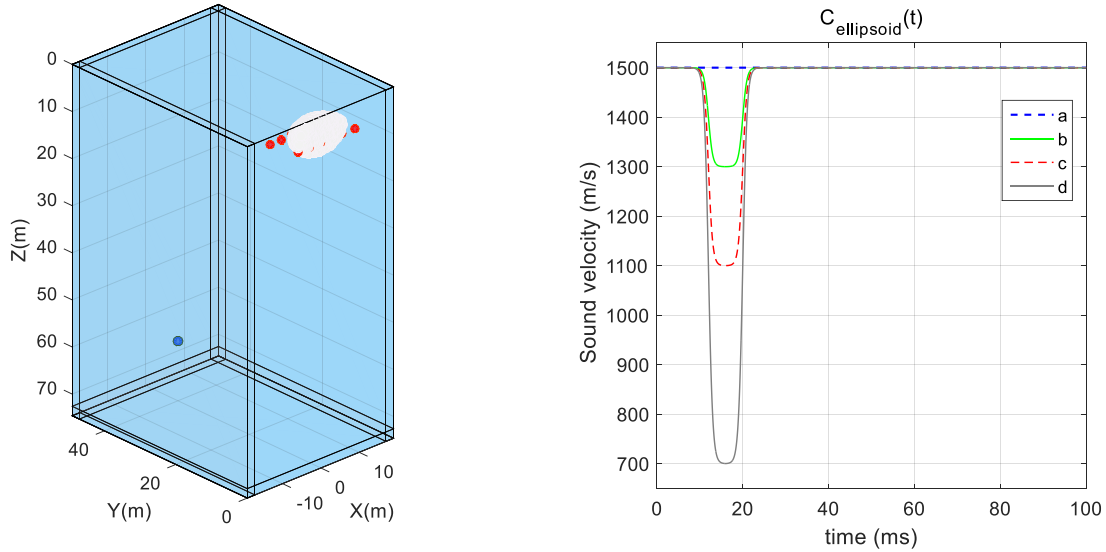
Figure 9 – (Left) The air-gun array is shown by red dots and the receiver by a blue dot. The fixed ellipsoid (Rx=6, Ry=5, Rz=3.5) centred at (Cx=0, Cy=0, Cz=4) resembling collection of cavities is shown in white near the source. (Right) The sound speed of the ellipsoid as a function of time for four different values. For case "a" sound velocity within the ellipsoid is constant and equal to that of water (1500 m/s). For "b", "c", and "d" the sound velocity is 1500 m/s before ~10 ms and after ~22 ms but between ~10 to ~22 ms drops to 1300, 1100, and 700 m/s, respectively.

The modelled pressure field snapshots at planes Y=0 (XZ plane) and X=0 (YZ plane) (Figure 5) at six time instants are shown for the case in which there is no sound velocity change in the ellipsoid (Figure 10) and when the sound velocity drops to 700 m/s (Figure 11).
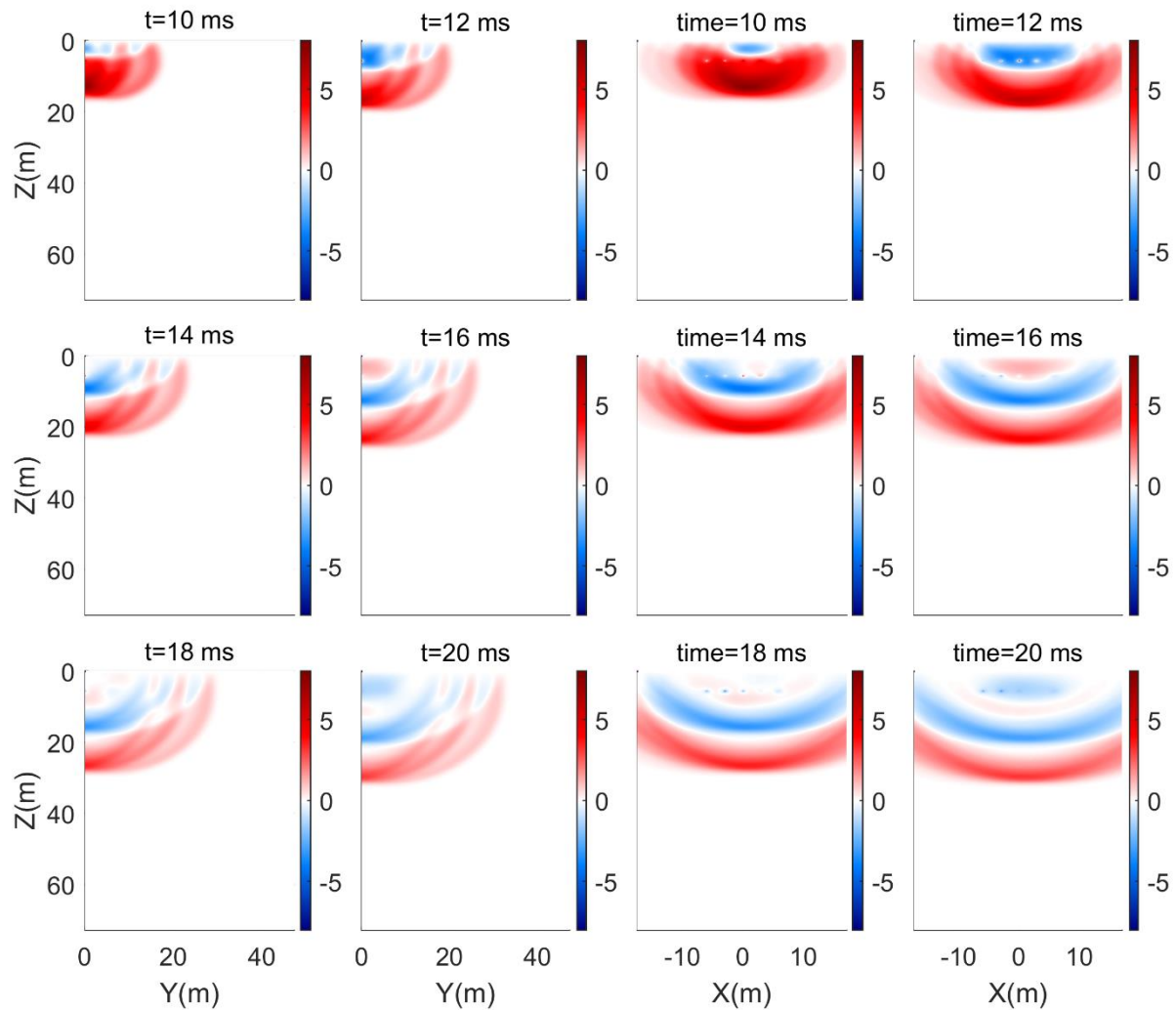
Figure 10 – Pressure field at six time instants on YZ and XZ planes (see Figure 5) for the case when the sound velocity within the ellipsoid remains the same as water. The colour-bar shows the acoustic pressure in bar.

The colour bar shows the acoustic pressure in bar. The red and blue colours represent positive and negative pressures, respectively. It is seen that the positive pressure reflected from the sea-surface becomes negative. Furthermore, the directionality of the air-gun array is observed which directs more acoustic energy downwards than horizontally. In this figure, the sound velocity of the whole computational domain is 1500 m/s and it is time-independent. If the sound velocity within the ellipsoid drops, then part of the incident wave will be reflected with opposite polarity. The pressure fields for this case are shown in Figure 11 where the ellipsoid sound velocity drops to 700 m/s for times between 12 and 20 ms (which corresponds to ~10 to ~18 ms after the array is fired). The

effects of local change in the medium are observed as pressure field differences between Figure 10 and Figure 11 for the time interval between 14 and 20 ms.
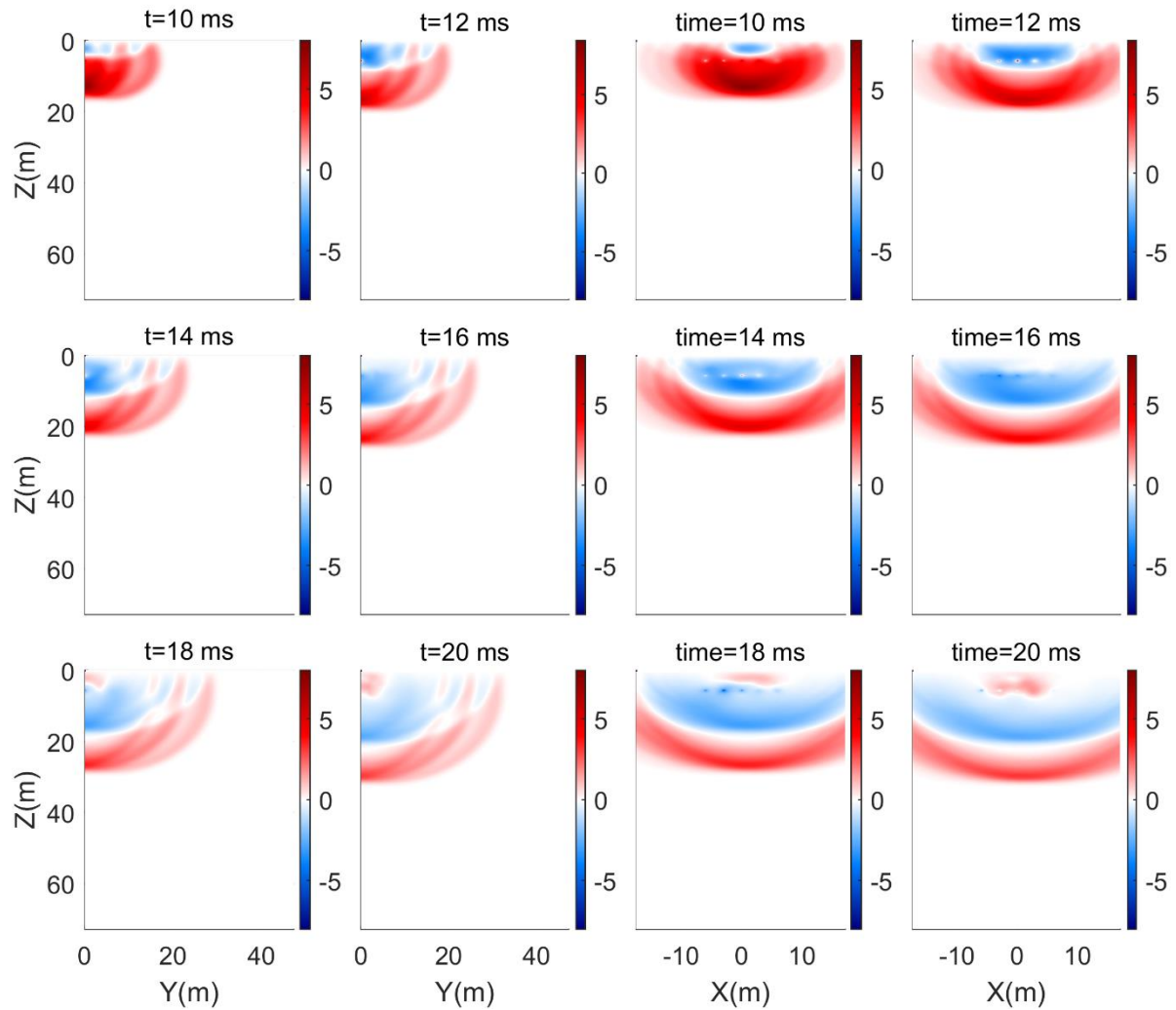


Figure 11 – Pressure field at six time instants on YZ and XZ planes (see Figure 5) for the case when the sound velocity within the ellipsoid drops to 700 m/s for a short time as shown by gray solid line in Figure 9 (right). The colour-bar shows the acoustic pressure in bar.

To see the effects of the sound velocity reduction within the ellipsoid on the pressure fields, the difference between the pressures shown in Figure 10 and Figure 11 are plotted in Figure 12.
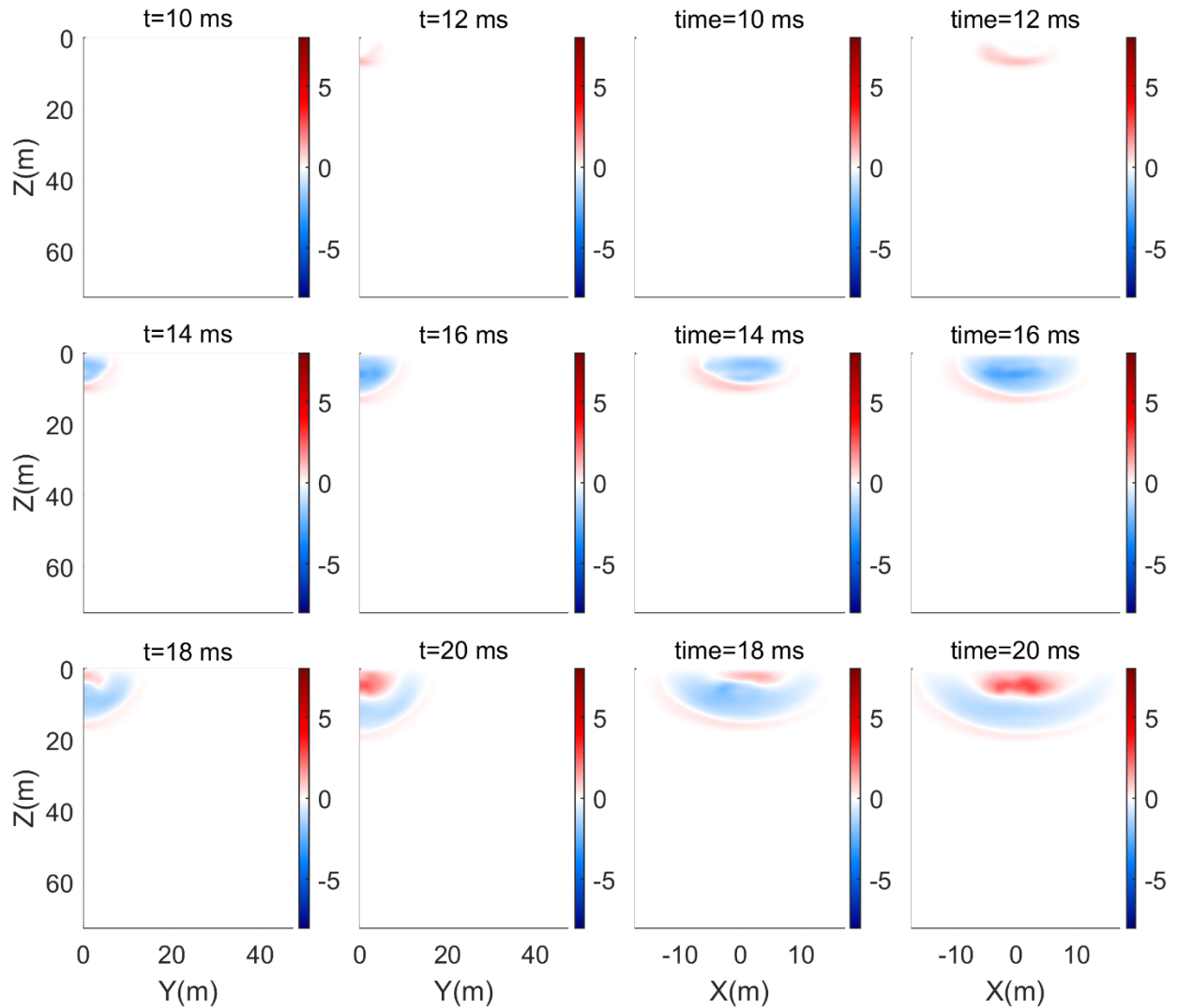
Figure 12 – Difference between Pressure fields on YZ and XZ planes shown in Figure 10 and Figure 11.

In addition to changing the sound velocity within the ellipsoid to 700 m/s, it was also changed to 1100 and 1300 m/s and the received acoustic pressure was simulated. The simulation results are plotted in Figure 13 together with the recorded field experiment.
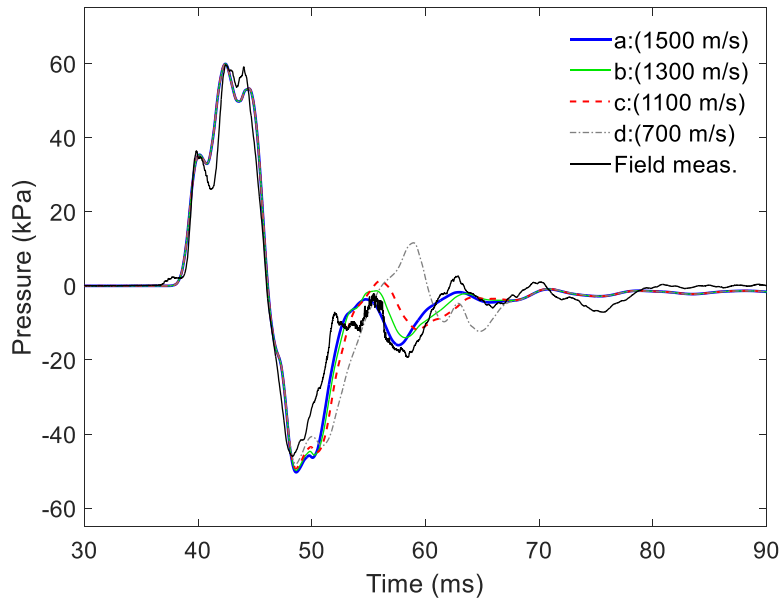
Figure 13 – The simulated pressure at receiver location for the case when sound velocity within the ellipsoid shown in Figure 5 (left) remains the same as water (1500 m/s) (a), drops to 1300 m/s (b), 1100 m/s (c), 700 m/s (d). The recorded pressure in the field experiment is also shown by a solid black line.

The blue solid line is for the case when the ghost cavity cloud does not change the sound velocity of the medium. It has the best agreement with the recorded field measurement signal shown by black colour. It is seen that reducing the sound velocity within the ellipsoid deteriorate the match between simulated and measured field data. Further reducing the sound velocity makes the correspondence poorer. We will elaborate on this observation in the discussion.

## 6.2. Cavity cloud modelling based on modelled pressure values

In this section, unlike the previous section where the cavity cloud was considered to be a fixed ellipsoid, it is assumed that cavities will grow at regions where the pressure (hydrostatic + acoustic pressure) drops below -0.1 bar. It should be noted that pressure values below zero are physically impossible. However, the air gun modelling software is based on the linear superposition of the ghost signals created by all the guns in the array, and hence the software will predict unphysical pressure values. We can use these artificial negative pressure values as constraints to predict the regions where cavity creation is likely to occur. The case where the sound velocity within the

cavity cloud drops to 900 m/s is shown in Figure 14 for four time instants. It is observed that the shape of cloud changes over time. To prevent numerical instabilities, the sudden change in the medium properties should be avoided. Therefore, the implementation of this case is more challenging compared to modelling the cavity cloud as a fixed ellipsoid as shown in the previous section.
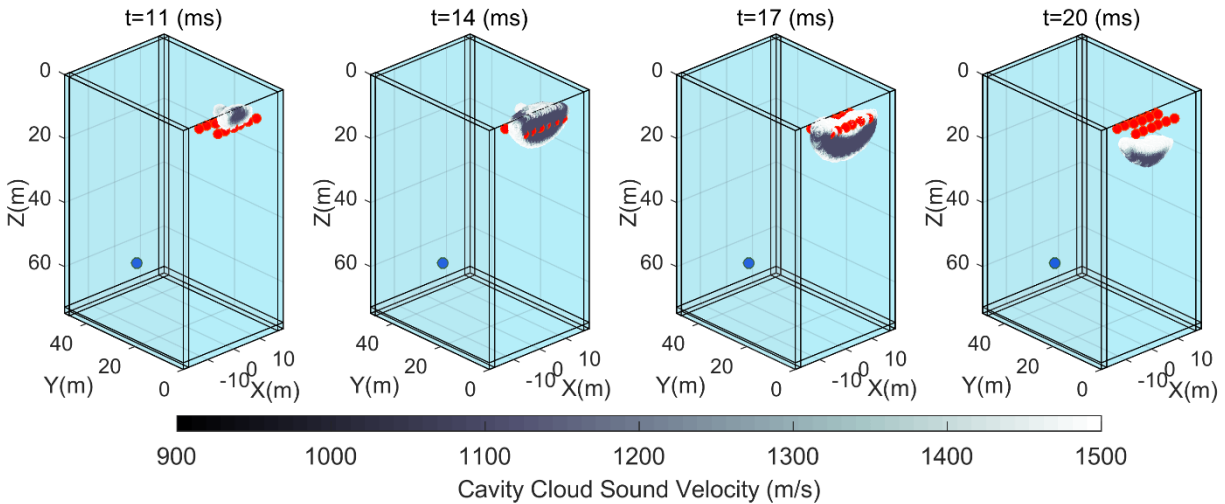


Figure 14 – Modelled cavity cloud at four time instants where the pressure drops below -0.1 bar. In this case it is assumed that the sound velocity within the cavity cloud reduces to 900 m/s. The blue dot shows the receiver.

The regions which contain cavities are then considered as a time-variant effective medium with acoustic properties different from the host medium. That is, the sound speed of grid points which satisfy the conditions for cavity growth is temporarily reduced to a certain level. The sound velocity reduction occurs within a short transition time using a sigmoidal shape function. Different values are assigned to sound velocity of the cavity cloud: 1300 m/s, 1100 m/s, 900 m/s and no sound velocity drop. For the case where the sound velocity of the cavity cloud drops to 900 m/s, Figure 15 shows the pressure field for six time instants at the Y=0 plane (XZ) and X=0 plane (YZ).
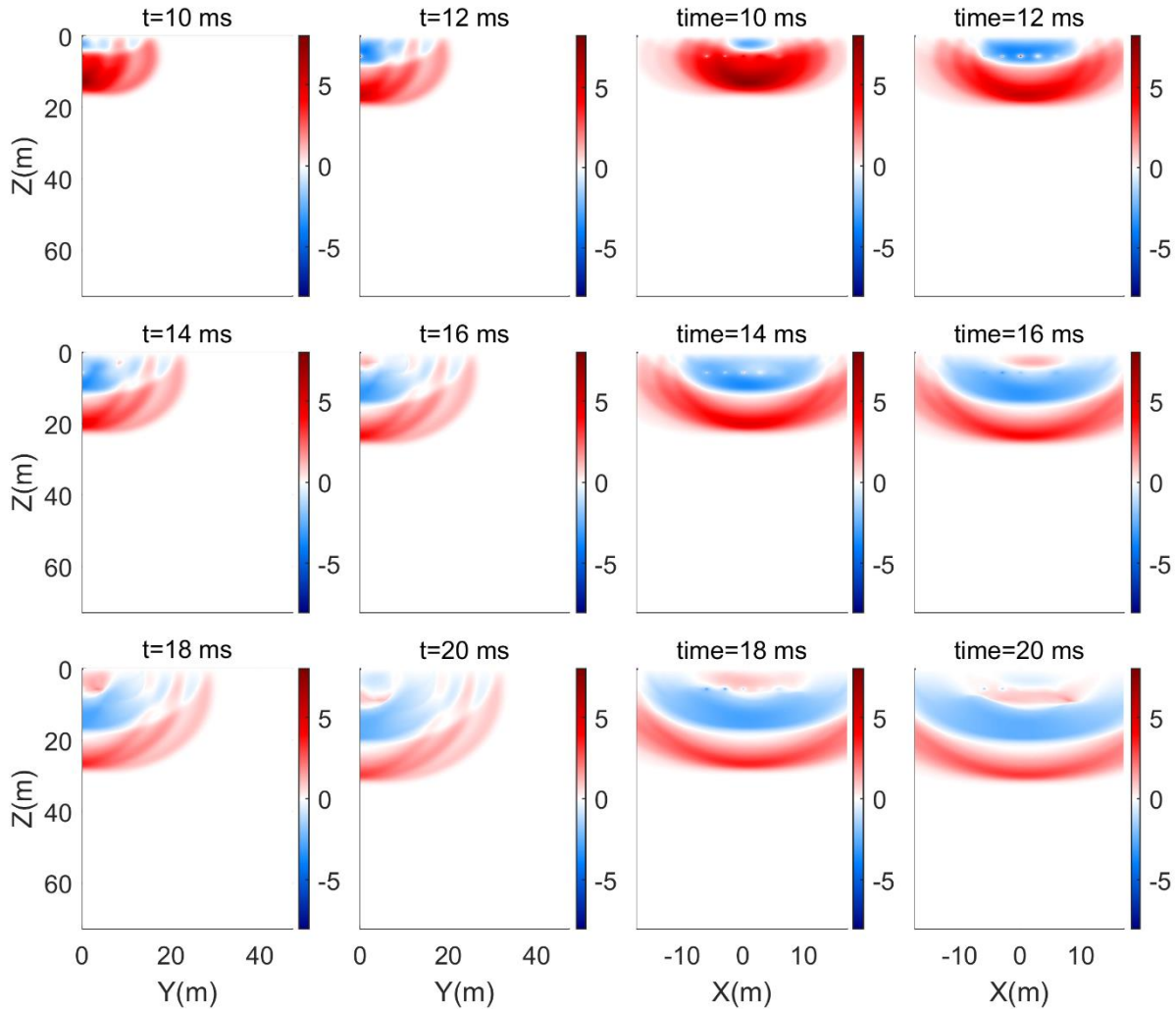
Figure 15 – Pressure field at six-time instants on YZ and XZ planes (see Figure 5) for the case when sound velocity within the cavity cloud drops to 900 m/s. The cavity cloud forms at locations where the pressure (hydrostatic + acoustic pressure) falls below -0.1 bar and diminishes when the pressure increases above this threshold.

Since the medium properties change differently compared to the fixed ellipsoid case, the pressure fields in this case (Figure 15) are different compared to the previous cases as was shown in Figure 10 and Figure 11. The simulated acoustic pressure at the receiver point for different values of sound velocities within the cavity cloud are shown in Figure 16. As for the previous case, including the sound velocity drop within the cavity cloud worsens the match between simulated and field measurements. The possible explanations for this observation are given in the discussion.
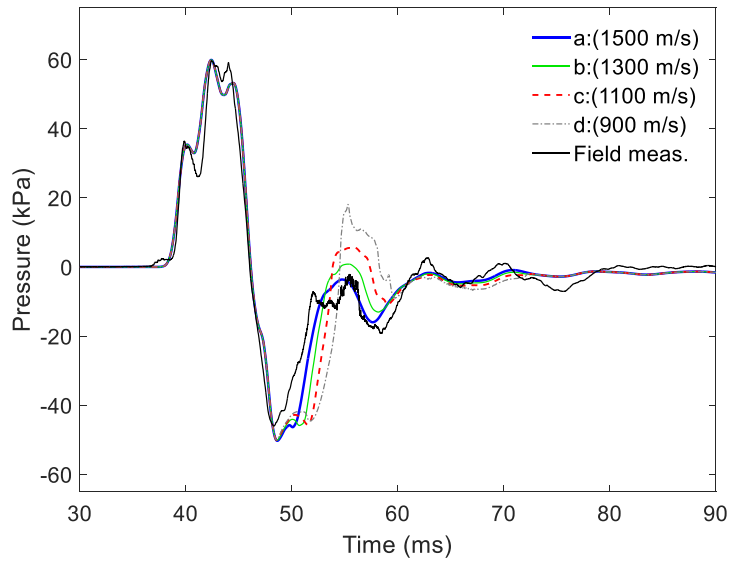
Figure 16 – The simulated pressure at receiver location for different values of sound velocity within the cavity cloud. The cavity cloud forms at locations that the pressure drops below -0.1 bar and diminishes when the pressure increases above this threshold. Sound velocity values within the cavity cloud drops to: 1500 m/s (the cavity cloud has no diffraction effect), (b) 1300 m/s, (c) 1100 m/s, and (d) 900 m/s. The recorded pressure in the field experiment is shown by a solid black line.

## 6.3.Including ghost cavitation signal in the modelling

Simulations show that the signal due to collapse of multiple cavities within the cavity cloud contains low frequencies in addition to the high frequencies (Khodabandeloo and Landrø, 2017a,b). The ghost cavitation signal is simulated (Khodabaneloo et al., 2017, Khodabandeloo and Landrø, 2017a) and plotted by purple dashed-dotted line in Figure 17 and the rest of the curves are generated by adding this signal to the curves in Figure 13.
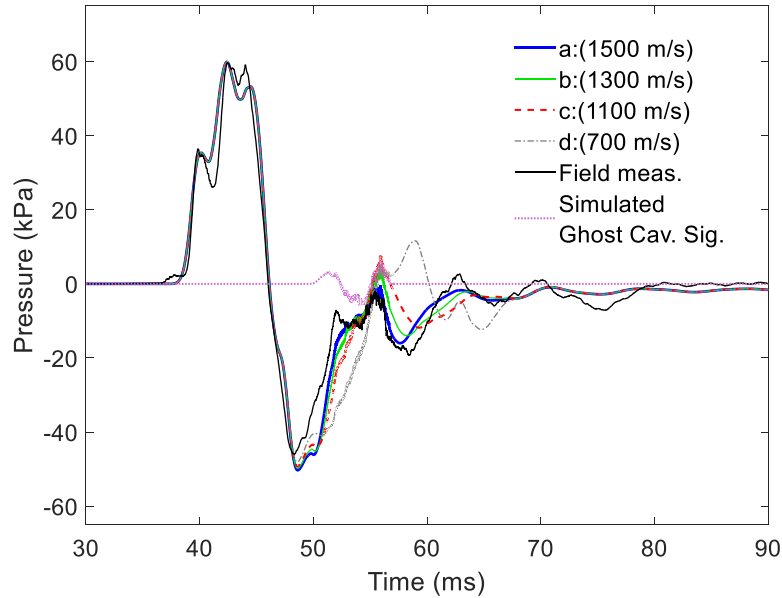
Figure 17 – The simulated pressure at receiver location + simulated ghost cavitation signal for the case when sound velocity within the ellipsoid shown in Figure 5 (left) remains same as water (1500 m/s) (a), drops to 1300 m/s (b), 1100 m/s (c), 700 m/s (d). The recorded pressure in the field experiment is also shown by solid black line.

It is observed that adding the effects of ghost cavitation signal to the far-field array signatures best matches for the case when sound velocity of cavity cloud – represented by ellipsoid – is the same as the surrounding water. There will be a poorer correspondence between the simulation and field data when the sound velocity within the ellipsoid is decreased. The same conclusion will be drawn if we add the simulated ghost cavitation signal to curves plotted in Figure 16. This means that the drop of the sound velocity within the cavity cloud deteriorates the correspondence between simulated far-field and field recorded signatures.

## 7. DISCUSSION

The cavity cloud is modelled as an effective medium with smaller sound velocity than water or air. Attenuation is not included within the cavity cloud. For 1% void fraction, ($\beta = 0.01$), in the frequency range of our problem the attenuation is around 1 dB/m (Zhang et al., 2017). In our case, as is discussed below, the void fraction is 4 to 5 orders of magnitude lower. Due to this fact and considering that the size of the cloud does not exceed a few meters, the attenuation effects of the cavity cloud is expected to be negligible and therefore it is ignored in our modelling.

Simulation results indicate that even 10-15% decrease in the sound velocity of medium for a short time in a small part of the medium around the air-gun array slightly affects the far-field recorded acoustic pressure. Comparing the simulation results to the field measurements suggests that the acoustic properties within the ghost cavity could not be significantly different from those of the surrounding water. It seems reasonable to assume that and the sound velocity within the cavity cloud should be larger than ~1300 m/s and this range is shown by a green rectangle in Figure 2. Then, depending on the vapour content of the cavities, the cavity volume fraction can be estimated from Figure 2: it is less than ~$1.6 \times 10^{-7}$ for 0.99 vapour fraction, while it is less than ~$7 \times 10^{-7}$ for 0.95 vapour fraction, and less than ~$1.6 \times 10^{-5}$ for pure gas ($Y_0$).

On the other hand, it is possible to roughly estimate the upper bound for the number of cavities ($N_{max}$) and the volume fraction of vapour cavities based on the amount of the acoustic energy on a plane located horizontally at depth $z_0$ (Figure 18), shown by $E_a|_{z_0}$, that can induce cavitation. It can be estimated using the following formula for the acoustic energy created by the down-going wave that has been reflected at the free surface:

$$E_a|_{z_0} = \int_A \int_{t_1}^{t_2} \frac{P^2\big((x,y,z=z_0),t\big)}{\rho_0 c} dt dA. \tag{12}$$

In the above formula, $P\big((x,y,z=z_0),t\big)$ is the portion of the acoustic pressure on a plane at depth $z_0$ that has potential to create cavities. That is the amount of the acoustic pressure which drops the pressure below the assumed threshold pressure (e.g. -0.1 bar). The time interval of the integration, $t_1$ to $t_2$, is the time when P drops below the threshold limit for cavitation generation and the area on the plane where the pressure is low enough for cavity generations is given by $A$. For the array configuration given in this paper, the maximum value of $E_a$ is found at the depth of 3.8 meters and is estimated to be 1194 Joules. The pressure values that drop below the threshold on the plane at depth $z_0$ =3.8 m are shown in Figure 18 at four time instants.
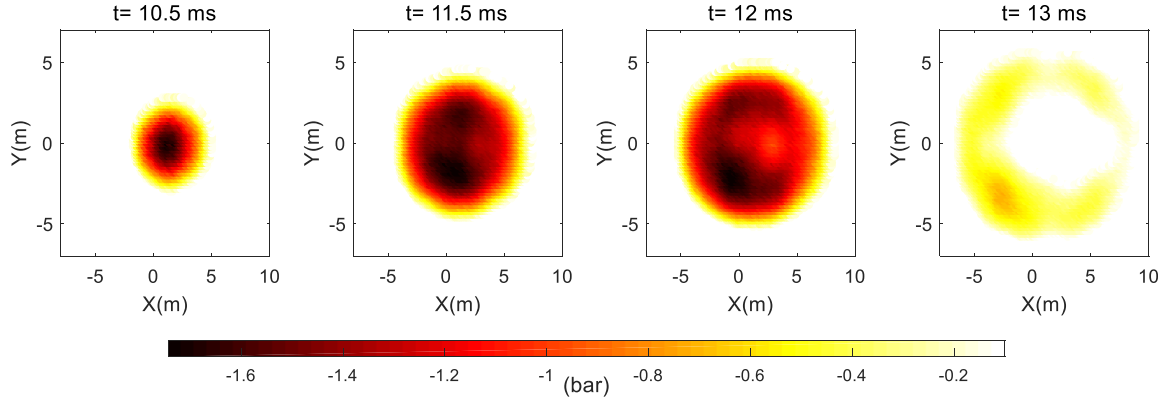
Figure 18 – Pressure values at four time instants that drop below -0.1 bar (i.e. the assumed threshold pressure for cavity generation) on a horizontal plane located at depth $z_0$=3.8m (shown schematically by green in Figure 19).

The maximum number of cavities $N_{max}$, can be estimated as:

$$N_{max} = \frac{E_a}{p_h V}.$$  (13)

Where $p_h$ is the hydrostatic pressure at the assumed depth (=3.8 m), and $V$ is the average volume of each cavity. Assuming an average cavity radius 3 mm, $N_{max}$ = 76926. For a cloud as an ellipsoid with dimensions of Rx=6 m, Ry=5 m, Rz=3.5 m, the corresponding maximum volume fraction of vapour cavities, $\beta_{max} = N_{max} V$, is estimated to be ~$2 \times 10^{-5}$, regardless of assumed cavity sizes. We emphasise that this is a rough estimation for the maximum possible volume fraction of vapour cavities within the cloud. It is observed that the estimated volume fractions from the far-field acoustic recordings given in this paper, are below this limit which is a confirmation of the results.

Using $\beta_{max}$ = ~$2 \times 10^{-5}$ and assuming the vapour fraction $Y_0 = 0.99$ the sound velocity within the cavity cloud is estimated as 225 m/s (shown by point A) in Figure 2. However, the far-field acoustic recording indicates that the sound velocity of the cavity cloud is not expected be less than ~1300 m/s (shown by green rectangle in Figure 2), on the basis of our analysis. Therefore, the other possibility is that the vapour content of the cavities is very low (Point C in Figure 2) to have sound velocity close to ~1300 m/s for $\beta_{max}$ = ~$2 \times 10^{-5}$. In other words, cavities are filled with air which seems not to occur physically. If we assume that most of the acoustic energy that can induce cavitation is maintained, it means that the number of cavities (hence β) in reality is probably significantly less than this. Reducing the $\beta_{max}$ by two orders of magnitude, $\beta_{(2)}$ = ~$2 \times 10^{-7}$ is obtained, which gives the sound velocity equal to 1250 m/s for a vapour fraction of 0.99 (shown

27

by point B). This is close to the estimated minimum sound velocity of the cloud based on comparison between measured and modelled far-field recordings.

In the ghost cavitation modelling with the same grid resolution as we used here, the initial number of cavities were scaled by the factor of 0.07 (Khodabandeloo and Landrø, 2017a) to match the measured field data. Then for a vapour fraction $Y_0=0.99$, the mean cavity radii must be $r = (0.2^3 \cdot 10^{-7}/(0.07 \cdot \pi \cdot 4/3))^{1/3} = 1.6$ mm to have the volume fraction less than $\sim 1.6 \times 10^{-7}$ and for $Y_0=0.95$ it must be 2.7 mm to have the volume fraction less than $\sim 7 \times 10^{-7}$.

The array studied in the example in this paper produces less than half the ghost cavitation compared to another array with almost same seismic energy but different air-gun arrangement (Khodabandeloo and Landrø, 2017b). Hence, for the arrays with stronger ghost cavity cloud than the one in our example, sound velocity reduction within the cloud can be a source of deviation between modelled and measured source array signature after the reflected ghost occurs.

To characterize the acoustic properties of a cavity cloud we suggest an experiment which is schematically shown in Figure 19. Two acoustic transducers, one well above and the other beneath the air-guns, are required to generate harmonic pressure waves. A hydrophone is required to be mounted below the acoustic transducer 2 to receive the generated acoustic wave by the transducers.
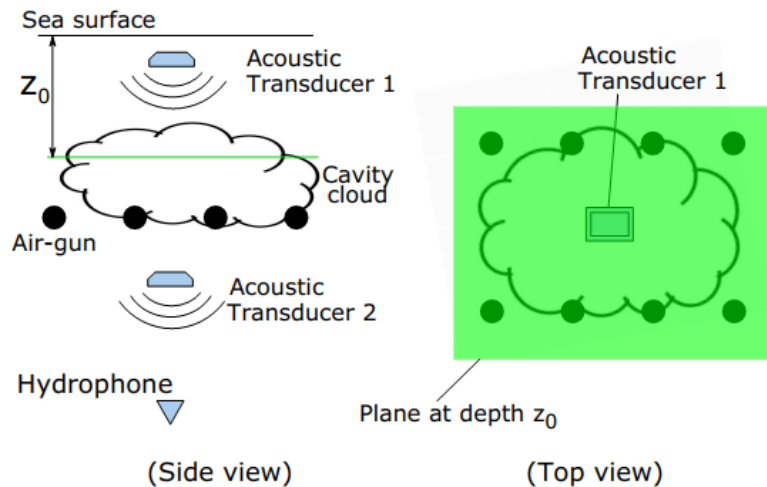


Figure 19 – The schematic of proposed test setup to characterize the acoustic properties of ghost cavity cloud. (left) side view of the test setup and (right) top view. The green plane located at depth $z_0$ (shown to the right) is included to explain equation (12).

In the first set of experiments, while transducer 2 is inactive, transducer 1 should generate a harmonic wave with a frequency above the seismic frequency band. This allows the use of filters to separate the acoustic signal from the transducer from the air-gun(s) pressure signal received by the hydrophone. The transducer should generate harmonic wave continuously for several, e.g. 20, air-gun shots. In the second set of experiments, the only difference is that transducer 2 is active and generates a harmonic wave as in the first set of experiments while transducer 1 is inactive. The second set of experiments are required to investigate the possible effects of air-gun pressure field on the transducers. For example, we may observe that in the first experiment the amplitude of the received harmonic wave by the hydrophone weakens when the ghost cavity cloud is expected and recovers afterward. This can be due to either the reflection of acoustic waves reaching the cavity cloud or the impact of air-gun pressure waves on the performance of the transducer. The second experiments help to remove these uncertainties. Since the air-guns generate strong acoustic waves, to avoid the saturation of received signals one solution is to have the hydrophone far enough below the air-guns.

## 8. CONCLUSION

Effects of sound velocity drop within the ghost cavitation cloud on the far-field recorded acoustic pressure is numerically simulated. The modelled cavity cloud appears around 10 ms after the air-gun array is fired and lasts for approximately 9 ms. This is confirmed by high-speed video recording. Wave propagation in a non-stationary (time-dependent) medium is modelled using k-wave modelling algorithm which is a k-space pseudo-spectral numerical method to solve the acoustic wave equation. A few modifications are applied to the source code to accommodate the time-dependent sound velocity of the medium. Modelling results are compared to the recorded field data. When there is no sound velocity drop within the cavity cloud, there is a good correspondence between the simulation results and the recorded field data. The simulation results indicate that even a 10-15% sound velocity drop within the cavity cloud lasting for only 8-10 ms, influences the far-field acoustic recordings. It is observed that if sound velocity within the cavity cloud drops below ~1300 m/s, the correspondence between the modelled acoustic signature and field measurement worsens. This means that it is very likely that for the present field data example, the velocity drop within the cavity cloud is less than 10%. From these observations the cavity volume fraction can be estimated depending on the cavity vapour content using Figure 2. For

example, the cavity volume fraction is less than $\sim 8 \times 10^{-7}$ and $\sim 1.6 \times 10^{-7}$ for 95% and 99% vapour fraction within the cavities, respectively.

## ACKNOWLEDGMENT

## REFERENCES

Barclay, F.I., Ledwedge, T.J., & Cornfield, G.C., 1969. Some Experiments on Sonic Velocity in Two-Phase One-Component Mixtures and Some Thoughts on the Nature of Two-Phase Critical Flow, *Proc., Inst. of Mechanical Engineering* **184**(3C) 185-91.

Commander, K.W. and Prosperetti, A., 1989. Linear pressure waves in bubbly liquids: Comparison between theory and experiments. *J. Acoust. Soc. Am.*, **85**(2), 732-746.

Cox, B.T., Kara, S., Arridge, S.R. & Beard, P.C., 2007. k-space propagation models for acoustically heterogeneous media: Application to biomedical photo-acoustics. *J. Acoust. Soc. Am.*, **121**(6), 3453-3464.

Domenico, S.N., 1982. Acoustic wave propagation in air-bubble curtains in water—Part I: History and theory. *Geophysics*, **47**(3), 345-353.

Fuster, D. & Montel, F., 2015. Mass transfer effects on linear wave propagation in diluted bubbly liquids. *J Fluid Mech*, **779**, 598-621.

Hamilton, E.L., 1978. Sound velocity–density relations in sea-floor sediments and rocks. *J. Acoust. Soc. Am.*, **63**(2), 366-377.

Kieffer, S.W., 1977. Sound speed in liquid-gas mixtures: Water-air and water-steam, *J. geophys. Res*, **82**(20), 2895-2904.

Khodabandeloo, B. and Landrø, M., 2018. Acoustically induced cavity cloud generated by air-gun arrays—Comparing video recordings and acoustic data to modeling. *J. Acoust. Soc. Am.*, **143**(6), pp.3383-3393.

Khodabandeloo, B., Landrø, M. & Hanssen, A., 2017. Acoustic generation of underwater cavities—Comparing modelled and measured acoustic signals generated by seismic air gun arrays. *J. Acoust. Soc. Am.*, **141**(4) 2661-2672.

Khodabandeloo, B. & Landrø, M., 2017a, June. Effects of Ghost Cavity cloud on Near-field Hydrophones Measurements in the Seismic Air Gun Arrays. In 79th EAGE Conference and Exhibition 2017., Paper Tu A4 09

Khodabandeloo, B. & Landrø, M., 2017b. High frequency ghost cavitation-a comparison of two seismic air-gun arrays using numerical modelling. *Enrgy. Proced.*, **125**, 153-160.

La Prairie, A.J.C., Method of Blasting: U.S. Patent No. 2699117, 1955.

Landrø, M., Amundsen, L., & Barker, D. 2011. High-frequency signals from air-gun arrays, *Geophysics* **76**(4), Q19–Q27

Landrø, M., Amundsen, L. & Langhammer, J., 2013. Repeatability issues of high-frequency signals emitted by air-gun arrays High-frequency air-gun signals. *Geophysics*, **78**(6), P19-P27.

Landrø, M., Ni, Y., & Amundsen, L. 2016. Reducing high-frequency ghost cavitation signals from marine air-gun arrays, *Geophysics* **81**(3), P33–P46

Lee, K.M., Hinojosa, K.T., Wochner, M.S., Argo, T.F., Wilson, P.S. & Mercier, R.S., 2011. Sound propagation in water containing large tethered spherical encapsulated gas bubbles with resonance frequencies in the 50 Hz to 100 Hz range. *J. Acoust. Soc. Am.*, **130**(5), 3325-3332.

Leighton T.G., 1994. The Acoustic Bubble (Academic, San Diego, 1994), pp 258-278.

Liu, Q.H., 1998. The pseudospectral time-domain (PSTD) algorithm for acoustic waves in absorptive media. *IEEE Trans. Ultrason., Ferroelect., Freq. Control*, **45**(4), 1044-1055.

Lucke, K., Lepper, P.A., Blanchet, M.A. & Siebert, U., 2011. The use of an air bubble curtain to reduce the received sound levels for harbor porpoises (Phocoena phocoena). *J. Acoust. Soc. Am.*, **130**(5), 3406-3412.

Medwin, H., 1977. In situ acoustic measurements of microbubbles at sea. *J. geophys. Res.*, **82**(6), 971-976.

Mellen, R. H., 1954. Ultrasonic spectrum of cavitation noise in water, *J. Acoust. Soc. Am.* **26**(3), 356–360.

Neppiras, E.A., 1984. Acoustic cavitation series: part one: Acoustic cavitation: an introduction. *Ultrasonics*, **22**(1), 25-28.

Nobes, D.C., Villinger, H., Davis, E.E. and Law, L.K., 1986. Estimation of marine sediment bulk physical properties at depth from seafloor geophysical measurements. *J Geophys. Res. Sol. EA*, **91**(B14), 14033-14043.

Pierce, A.D., 1989. *Acoustics: an introduction to its physical principles and applications*. Acoustical Society of America, Huntington Quadrangle Melville, NY.

Plesset, M.S., 1970. Effect of dissolved gases on cavitation in liquids (No. 85-55), California Institute of Technology, Pasadena Division of Engineering and Applied Science.

Prosperetti A., 2015. The speed of sound in a gas–vapour bubbly liquid. *Interface Focus* **5**: 20150024. http://dx.doi.org/10.1098/rsfs.2015.0024

Prosperetti, A., 2017. Vapour bubbles. *Annu Rev Fluid Mech*, **49**, 221-248.

Rienstra, S. W., & Hirschberg, A., 2015. *An Introduction to Acoustics*, Eindhoven Univ. of Technology, Eindhoven, pp. 15–19, 68–70

Ross, W.S., Lee, P.J., Heiney, S.E., Young, J.V., Drake, E.N., Tenghamn, R. & Stenzel, A., 2005. Mitigating seismic noise with an acoustic blanket—the promise and the challenge. *The Leading Edge*, **24**(3), 303-313.

Silberman, E., 1957. Sound velocity and attenuation in bubbly mixtures measured in standing wave tubes. *J Acoust. Soc. Am.*, **29**(8), 925-933.

Tabei M., T. D. Mast, & R. C. Waag, A., 2002. k-space method for coupled first-order acoustic propagation equations, *J. Acoust. Soc. Am.*, **111**(1), 53–63.

Treeby, B.E., & Cox. B.T., 2010. k-Wave: MATLAB toolbox for the simulation and reconstruction of photoacoustic wave-fields, *J Biomed Opt*, **15**(2), 021314-12.

Treeby B. E., Jaros J., Rendell A. P., & Cox, B.T., 2012. Modelling nonlinear ultrasound propagation in heterogeneous media with power law absorption using a k-space pseudospectral method, *J. Acoust. Soc. Am.*, vol. **131**(6) 4324-4336.

Wilson, P.S. & Roy, R.A., 2008. An audible demonstration of the speed of sound in bubbly liquids. *Am. J. Phys.*, **76**(10), 975-981.

Wood, A. B. 1946. *A Textbook of Sound*. London: G. Bell and Sons Ltd.

Würsig, B., Greene, C.R. & Jefferson, T.A., 2000. Development of an air bubble curtain to reduce underwater noise of percussive piling. *Mar. Environ. Res.*, **49**(1), 79-93.

Yee, K., 1966. Numerical solution of initial boundary value problems involving Maxwell's equations in isotropic media. *IEEE Trans. Antennas Propag*, **14**(3), 302-307.

Zhang, Y., Guo, Z., Gao, Y. & Du, X., 2018. Acoustic wave propagation in bubbly flow with gas, vapour or their mixtures. *Ultrason. Sonochem.*, **40**, 40-45.